Pergamon

Int. J. Heat Mass Transfer. Vol. 37, No. 16, pp. 2425–2438, 1994

0017-9310/94 $7.00 + 0.00

0017-9310(94)E0061-X

Natural convection flow and heat transfer within a rectangular enclosure containing a vertical porous layer

M. SONG and R. VISKANTA†

Heat Transfer Laboratory, School of Mechanical Engineering, Purdue University, West Lafayette, IN 47907, U.S.A.

(*Received* 10 *October* 1993 *and in final form* 4 *March* 1994)

Abstract—An experimental and theoretical study of natural convection flow and heat transfer within a rectangular enclosure partially filled with an anisotropic porous medium is conducted as a step to understand the effects of the mushy region flow characteristics on the interacting flows of the melt pool and the mushy zone of solidifying alloys. The test cavity is filled with a porous medium for half the lateral distance to the cold wall and is heated and cooled at the vertical end walls by imposing uniform but different temperatures. The solid matrices of the porous media are constructed with perforated plates, and measured flow characteristics are used in the predictions. Flow visualization in the porous region is made possible by the latticed structure of the porous matrices and electrolysis dye generation. The effect of anisotropic flow characteristics of the porous medium on the flow and heat transfer is modeled mathematically using volume-averaged conservation equations. The mathematical model was validated by comparing the predicted velocity and temperature fields with the visualized streamlines and measured temperatures. To investigate the effect of anisotropic permeability for wider ranges of dimensionless parameters, numerical experiments were conducted. The importance of incorporating the mathematical models which account for the anisotropic characteristics of the mushy zone is emphasized.

INTRODUCTION

NATURAL convection flow and heat transfer in a system containing simultaneously a fluid reservoir and a porous medium, saturated with the same fluid as that of the reservoir, is of considerable theoretical and practical interest. Applications include solidification of ingots and castings, crude-oil production, ground water pollution, porous insulations, geophysical systems, etc. For example, when a porous insulation occupies only a fraction of the space between two walls, the fluid flow and heat transfer can be significantly reduced due to the large frictional resistance offered by the porous insulation. Penetration of fluid into a porous medium is also important in solidifying castings [1]. During the solidification of the off-eutectic composition alloy, a mushy zone exists consisting of a fine mesh-work of dendrites growing into the melt, owing to the solubility difference between the solid and liquid phases and the extended freezing temperature range. Fluid flow between the porous mushy zone and the pure melt region can alter the chemical homogeneity and the grain structure of the final product.

A comprehensive review of the literature on the subject of natural convection fluid flow and heat transfer in porous media is available [2] and need not be repeated here. Among the large variety of configurations, the more complex solid matrices, having inhomogeneous and anisotropic characteristics, are of greater interest to practical applications, since real porous media, either natural or artificial, are rarely homogeneous and isotropic.

Non-homoneous porous media can be isotropic if the distribution of inhomogeneity is isotropic (isotropic medium with multiple hierarchy [3]), but most of the studies concerned with non-homogeneous media deal with the layered structures, and anisotropy normally accompanies such structure because the direction of inhomogeneity is distinct. On the other hand, considerable portion of anisotropic characteristics possessed by porous media has its origin in the periodically repeating arrangement of inhomogeneity. According to the numerical predictions by Gjerde and Tyvand [4], the critical Rayleigh numbers for the onset of convection in the alternating porous layers approach those of homogeneous anisotropic porous medium as the number of layers in the confinement is increased. The average heat fluxes for fibrous anisotropic media and alternating layers of glass fibers and glass cloth, however, show different trends in the experimental investigation of Castinel and Com-

† Author to whom correspondence should be addressed.

NOMENCLATURE

A	aspect ratio, L/H
B	fluid layer thickness [m]
b	dimensionless fluid layer thickness, B/H
c_P	specific heat [J kg^{-1} K^{-1}]
Da	D'Arcy number, K_o/H^2
f	inertial coefficient in Forchheimer extension
g	gravitational acceleration [m^2 s^{-1}]
H	height of enclosure [m]
k	thermal conductivity [W m^{-1} K^{-1}]
K	permeability [m^2]
L	length of enclosure [m]
Nu	Nusselt number, hL/k_f
P	pressure [Pa]
Pr	Prandtl number, v_f/α_f
Ra	Rayleigh number, $g\beta(T_H-T_C)H^3/(v_f\alpha_f)$
R_k	ratio of thermal conductivity, k_{eff}/k_f
R_P	ratio of permeability, K_o/K
R_μ	ratio of dynamic viscosity, μ_{eff}/μ_f
T	temperature [K]
U	x-component velocity [m s^{-1}]
V	y-component velocity [m s^{-1}].

Greek symbols

α	thermal diffusivity [m^2 s^{-1}]
β	coefficient of thermal expansion [K^{-1}]
ε	porosity
μ	dynamic viscosity [N s m^{-2}]
v	kinematic viscosity [m^2 s^{-1}]
ρ	fluid density [kg m^{-3}]

Subscripts

c	cold
eff	effective value
f	fluid
h	hot
o	standard value for Da
ref	reference condition
x	x-component
y	y-component.

barnous [5]. The validity of porous media models assuming periodically repeating non-identical porous layers as a homogeneous anisotropic porous media need further research attention to gain improved understanding of physical phenomena.

The configurations of porous layers which have been considered are diverse. The number of layers varied from two [6] to several [7–9] or more [4]. Different types of layer orientations against the direction of gravity and various thermal and hydraulic boundary conditions were tested experimentally and theoretically. The results show that inhomogeneous and anisotropic characteristics can significantly affect the flow structure and heat transfer. Generally, a stronger effect resulted when the product of Rayleigh number (Ra) and D'Arcy number (Da) was large and the permeability ratio of the adjacent layers deviated more from unity. When one of the layers is replaced with a fluid layer, local values of the Ra and Da product and the permeability ratio would be both infinity. The discussions deduced from the results of collateral porous layers cannot be extrapolated to these limiting cases, unless the porous medium models consider the advective (and diffusive) transport of momentum.

Systems containing a fluid layer and a homogeneous and isotropic porous layer have been studied by a number of investigators. The instability of natural convection for the system consisting of a horizontal porous layer saturated and overlaid with a fluid has been investigated utilizing the Brinkman extension of D'Arcy's law, when the system is heated from below [10] and when the system is volumetrically heated in the porous layer and is heated or cooled from below and/or from above [11, 12]. The review of the literature on the same subject can be found therein. Reda [13] also considered the horizontal porous and liquid-layers, but confined his attention to the concentric annular column where heating and cooling was occurring at the vertical walls. Due to the uncertainties in the effective viscosity, a simple D'Arcy model was adopted and discontinuity of a hydraulic boundary condition was unavoidable. Ellinger and Beckermann [14] reported an experimental study on the melting of N-octadecane within an enclosure heated and cooled at the vertical side walls and partially occupied by a horizontal porous layer. In the experimental and numerical studies by Beckermann *et al.* [15], a rectangular enclosure was filled with a vertical fluid layer and a homogeneous porous layer, and a horizontal temperature gradient was imposed. It was found that if the fluid penetrates into the porous layer, natural convection patterns in the entire enclosure are significantly altered compared to the fully porous or fluid filled enclosures. The same configuration, except that the porous layer may not border on the cold vertical wall, was investigated numerically by Arquis and Caltagirone [16], Beckermann *et al.* [17] and Du and Bilgen [18], and much the same conclusions were reached. Tong *et al.* [19] and Campos *et al.* [20] also studied a similar system but the interface between the fluid and porous layers was impermeable and the application was limited to thermal insulations.

Measured permeabilities of dendritic structures forming the porous mushy zone have been found to be highly inhomogeneous and anisotropic [21], while most of the studies devoted to the solidification of

mixtures assumed inhomogeneous but isotropic characteristics. West [22] has taken into account anisotropic permeabilities in the unidirectional solidification model. With a constant temperature condition imposed at the interface between the mushy zone and the melt pool, the energy equation was not solved in the mushy zone, and no results for anisotropic permeability were presented.

This paper reports on a study of natural convection flow and heat transfer within a rectangular enclosure, which is filled with an anisotropic porous medium for half the lateral distance to the cold wall and is heated and cooled at the vertical end walls by imposing uniform but different temperatures. The purpose of the study is to obtain fundamental understanding of the transport phenomena occurring in the melt pool and the mushy zone of solidifying alloys. Especially, the effects of anisotropic mushy region flow characteristics on the interacting flows of the melt pool and mushy zone is assessed under the simpler but controlled physical situation. Flow is driven by thermal buoyance force only and the medium does not undergo phase change. The mushy region is mimicked by a porous medium having the desired flow characteristics, which do not change with time. The solid matrix of the porous media is constructed, and its directional permeabilities are measured. Flow visualization in the porous region is made possible by the latticed structure of porous matrices and dye generation due to electrolysis. Temperature distributions are measured and compared with the predictions yielded by a mathematical model based on the volume-averaged conservation principles. The effect of anisotropic flow characteristics of the porous media in the flow and heat transfer is further investigated via numerical experiments over a wide range of model parameters.

EXPERIMENTS

Test cell and porous medium

The experiments were performed in two different rectangular test cells both with the inner dimensions of 148 mm in height and 74 mm in depth. The length of the cavity was either 148 mm or 308 mm corresponding to the aspect ratio of 1.0 and 2.08 each. The vertical front wall and back walls were made from two layers of 13 mm thick acrylic plates with a 13 mm thick air gap between the plates, and the horizontal top and bottom walls were made of 25 mm thick acrylic plates. The 50 mm thick Styrofoam insulation covered the outer surface of the acrylic walls, except for the brief moment while the photographs for flow visualization were taken. The vertical end walls of the test cell served as the hot and cold walls and were made of 6 mm thick copper plates. Water was circulated from the constant temperature bath (HAAKE A82) through the channels formed by the outer surface of the copper plates and the passages milled in the 33 mm thick carbon plastic plates. Each heat exchanger had three coolant passages extending over the upper, middle and lower thirds of the copper plates. The temperature distribution along the height of the copper plates could be maintained within ± 0.1 C of the desired values by adjusting the flow rate of each coolant passage. The five type-T thermocouples, equally spanned along the vertical centerline of each end wall and placed close to the surface contacting the cavity, ensured the uniform temperature boundary condition. The water-tight holes for thermocouples, electrodes and filling/draining lines were placed in the top and bottom walls. The test assembly, including the insulation, was placed on an aluminum plate with leveling screws.

The solid matrix of the porous medium occupying the half length of the test cavity had a rectangular latticed structure (Fig. 1), comprising permeable plates either horizonal or parallel with the end walls and equally spaced along the height or the length of the cavity. For the permeable plates, 3.18 mm thick polypropylene plates perforated with 2.38 mm dia. staggered-centered holes, were chosen among the few commercially available materials. The holes provided a 25% open area and were aligned to allow the insertion of thermocouples from the direction perpendicular to the permeable plates. The macroscopic characteristics of the porous media such as the permeabilities, porosities and effective thermal conductivities, when saturated with the designated fluid, were varied by changing the spacings of the permeable plates and are given in Table 1, together with the summary of the experimental conditions selected for the discussion. The detailed explanations of the porous matrixes configuration and of the measurements and analysis of the macroscopic properties are given by Song [23].

Test procedure

After the test cell and the solid matrix of the porous medium was assembled, the desired fluid was introduced into the cavity, and the temperature difference was imposed and maintained until the steady state was achieved. The saturating fluid was either pure water of 80% glycerol aqueous solution. In the preparation of the fluid, degassing was essential for two reasons: (1) to prevent the evolution of dissolved gases during the experiment, which would form an

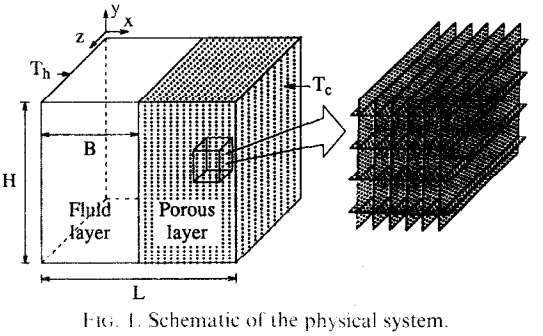

FIG. 1. Schematic of the physical system.

Table 1. Summary of experimental conditions $Da = 3.45 \times 10^{-7}$ ($K_0 = 6.95 \times 10^{-9}$ m^2)

	A	B	Fluid	T_h (°C)	T_c (°C)	Ra	Pr	ε	R_{px}	R_{py}	R_{kx}	R_{ky}
1	1.0	0.49	†	30	15	3.33×10^7	230	0.744	0.232	0.232	0.723	0.723
2	1.0	0.49	†	30	15	3.33×10^7	230	0.801	0.208	0.116	0.761	0.773
3	1.0	0.49	water	25	20	2.48×10^8	6.47	0.744	0.232	0.232	0.705	0.705
4	2.14	1.14	water	27.5	22.5	2.73×10^8	5.98	0.744	0.232	0.232	0.705	0.705
5	2.14	1.14	water	27.5	22.5	2.73×10^8	5.98	0.629	0.465	0.303	0.597	0.622
6	2.14	1.14	water	40	10	1.64×10^9	5.98	0.744	0.232	0.232	0.705	0.705

† 80% glycerol + water.

unwanted gas phase near the top wall or inside the porous media; and (2) to immediately dissolve the hydrogen and oxygen molecules produced during the electrolysis dye generation. As the fluid was siphoned into the cell for the test, it was heated above 90°C (50°C higher than the maximum hot wall temperature) and passed through a chamber where the evolved gas bubbles were separated. To prevent the air from being trapped in the porous medium and blocking the flow passage, the filling process was very slow (0.9 cm^3 s^{-1}) and 6 cc of wetting solution (KODAK Photo-Flo 200) was added. After the test cell was filled up, three times more volume of the fluid was passed to decrease the remaining amount of wetting solution, so that its effect on the thermophysical properties of the fluid is believed to be negligible.

The algebraic mean of the hot and cold wall temperatures were kept close to the room temperature (22.5–27.5°C) to reduce the heat loss/gain to the ambient environment. After the constant temperature baths were set, enough time (10 h; 99% of temperature change occurred during the first 5.3 h) was allowed before temperature measurements or flow visualizations were made. In the meantime, the flow rate of each coolant passage was adjusted to ensure the isothermal boundary condition at the end walls. The temperature distribution inside the enclosure was measured with nine type-K thermocouple probes, sheathed in a 1.63 mm O.D. stainless steel tube and having an exposed bead. All thermocouples including type-T at the heat exchangers were calibrated with an accuracy of ±0.1°C.

The flow visualization technique used was based on the pH variation due to the electrolysis and consequent coloration of phenolpthalein aqueous solution around the cathode [24]. The results of preliminary experiments to determine the minimum amount of chemicals to be added to water are given in Table 2. Sodium chloride concentration can be decreased further if a higher voltage source than this study (20 V) is employed. At each dye generating point, a 57 mm long stainles steel rod of O.D. 0.56 mm was placed along the depth of the test cavity and served as a cathode. Each cathode was supplied with 80 μA d.c. by a simple electric circuit, consisting of a resistor and one transistor, to generate equal amount of dye. As the electrolysis occurs, hydrogen and oxygen molecules are produced at the rate proportional to the current passed. When the fluid was degassed water, those molecules were dissolved immediately and up to 6 times of 30 min dye generations were possible with no buoyancy disturbance caused by the hydrogen bubbles. For the glycerol aqueous solution the larger amount of chemicals and current are required, since the coloration is poor due to the small water content. As the gas phase started to form around the electrodes before sufficient dye was generated, the present flow visualization technique is not appropriate for the aqueous glycerol solution with a water content less than 50%.

ANALYSIS

Model equations

A schematic of the physical model and coordinate system is shown in Fig. 1. The analysis assumes that the flow is steady, laminar and two-dimensional. While the formulation retains the form of incompressible flow, the volume expansion coefficient in the buoyancy term of the momentum equation is assumed to be constant. The fluid viscosity, thermal conductivity and specific heat are assumed constant, and the values at 25°C are used in evaluating dimensionless parameters. Also, it is assumed that the porous medium is homogeneous but the transport characteristics are anisotropic. Furthermore, for convenience the principal directions of the permeability tensor, K, and the effective thermal conductivity tensor, k_{eff}, are assumed to correspond with the coordinate axes. With the assumption of local thermal equilibrium and neglect of viscous heat dissipation, the volume-averaged model equations are as follows:

continuity:

$$\frac{\partial U}{\partial x} + \frac{\partial V}{\partial y} = 0, \tag{1}$$

Table 2. Components added to water for flow visualization

Component	Function	Concentration by weight
Phenolpthalein	pH indicator	2×10^{-5}
Ethyl alcohol	solvent	1×10^{-5}
Sodium chloride	electrolyte	2×10^{-4}

momentum:

$$\frac{\rho}{\varepsilon^2}\left(U\frac{\partial U}{\partial x}+V\frac{\partial U}{\partial y}\right)=-\frac{\partial P}{\partial x}+\frac{\partial}{\partial x}\left(\mu_f R_\mu\frac{\partial U}{\partial x}\right)+\frac{\partial}{\partial y}\left(\mu_f R_\mu\frac{\partial U}{\partial y}\right)-\frac{\mu_f}{K_o}R_{Px}U, \quad (2)$$

$$\frac{\rho}{\varepsilon^2}\left(U\frac{\partial V}{\partial x}+V\frac{\partial V}{\partial y}\right)=-\frac{\partial P}{\partial y}+\rho g\beta(T-T_{ref})+\frac{\partial}{\partial x}\left(\mu_f R_\mu\frac{\partial V}{\partial x}\right)+\frac{\partial}{\partial y}\left(\mu_f R_\mu\frac{\partial V}{\partial y}\right)+\frac{\mu_f}{K_o}R_{Py}V, \quad (3)$$

energy:

$$\rho C_{Pf}\left(U\frac{\partial T}{\partial x}+V\frac{\partial T}{\partial y}\right)=+\frac{\partial}{\partial x}\left(k_f R_{kx}\frac{\partial T}{\partial x}\right)+\frac{\partial}{\partial y}\left(k_f R_{ky}\frac{\partial T}{\partial y}\right), \quad (4)$$

where

$$\varepsilon = R_\mu = R_{kx} = R_{ky} = 1, \quad (5)$$

and

$$R_{Px} = R_{Py} = 0 \quad \text{for} \quad 0 \leqslant x \leqslant B. \quad (6)$$

Note that only the terms related to the diagonal components of the permeability tensor, **K**, and thermal conductivity tensor, **k**, are included. Since the principal directions of the permeability tensor are mutually orthogonal, the difficulties in applying the Forchheimer extension to the anisotropic porous medium are reduced, and it is incorporated utilizing the following relation [25]:

$$R_{Pq} = R_{Pqo}\left(1+f\frac{\sqrt{K_o/R_{Pqo}}}{\nu_f}\|\vec{\mathbf{V}}\|\right), \quad (7)$$

where

$$q = x, y \quad \text{and} \quad R_{Pqo} = [R_{Pq}]_{\|\vec{\mathbf{V}}\|\to 0} \quad \text{(D'Arcy model)}. \quad (8)$$

The inertial coefficient f was empirically evaluated to be 0.7 [22].

The analytical determination of the effective diffusion coefficients R_μ and R_k (dimensionless) is very complicated even for the simple geometries. The effective viscosity, μ_{eff}, has been evaluated from the statistical theory as a function of porosity for a dilute swarm of stationary monosized solid spheres, and empirically correlated as a function of permeability for flows parallel to the interface between the fluid and porous layer [26]. Considering the range of the parameters in this study, taking R_μ as unity reproduces the trend of the above data reasonably well. The same model for R_μ has yielded good agreement with experimental results in many studies [15]. Due to the lack of empirical models for the geometry constructed, the value of the effective thermal conductivities are calculated with the assumption of uniform temperature gradient (Table 1). Calculated values are 1.3–7.4% smaller compared to the values predicted by simple volume-averaging.

The boundary conditions for the continuity and momentum equations are of the no-slip type at the impermeable walls, and those for the energy equations are constant temperature and adiabatic conditions at the vertical and horizontal connecting walls, respectively. The governing equations for two different domains (the fluid reservoir and the porous medium) have the same form and can be expressed as one set as in equations (1)–(4), and so are the outer boundary conditions. However, the matching conditions at the interface of the two domains must be satisfied for the problem to be solved as a single domain. The jump in the volumetric porosity across the interface implies a jump in the area porosity, which is equal to the total area of fluid–solid segments along the interface. Volume-averaged velocities are continuous across the interface, because they are continuous on the fluid–solid segments as well as the fluid–fluid segments. For the same reason, temperature and heat flux are continuous at the interface. However, the stresses acting on the fluid–solid segments are not properly accounted for on the fluid side of the segments, if the macroscopic tangential stress is assumed to be continuous at the interface. For both the normal and tangential stresses to be continuous at the interface, the following additional assumptions are necessary [27]:

(1) the sum of advective and dispersive momentum fluxes across the interface is much smaller than the diffusive one; and
(2) the (macroscopic) viscous part of the fluid stress vectors across the boundary is negligible, when compared with the forces due to the pressure.

Method of solution

Since the model equations governing the velocity and temperature fields are of the conservation form, a coupled elliptic partial differential equation solver was utilized with modifications to handle the anisotropic diffusion coefficients. The model equations are discretized using the control volume formulation and are solved using the SIMPLEC algorithm [28]. The power law scheme and the harmonic-mean formulations are incorporated in evaluating the momentum/heat fluxes and the diffusion coefficients.

The main difficulties encountered were in dealing with the large Rayleigh numbers ($O \approx 10^9$, for the water filled enclosure having a characteristic length of 0.2 m with the temperature difference of few degrees). The validity of the laminar flow model is questionable. Two different sets of dimensionless equations, adopted by Henkes and Hoogendoorn [29] and Ozoe

et al. [20] in their turbulent flow models of natural convection along an infinite vertical wall and in a cavity were used. In spite of the order of magnitude differences in the dimensionless variables, solutions differed little and convergence behavior was the same and showed that the results were independent of the non-dimensionalization method used.

As the Rayleigh numbers are high, greater changes in the dimensionless variables occur near the impermeable walls and near the interface between the fluid reservoir and the porous medium. To accommodate the drastic changes, the distribution of the nodal points were skewed to have finer grid spacings near these boundaries. The ratio of adjacent cell dimensions were kept uniform at the value of 1.15 for 70×34 nodal points and 1.09 for 138×66 nodal points. Obviously, to decrease the cell Peclet numbers $[\rho U_p(\Delta x)/\Gamma]$ throughout the calculation domain, a larger number of nodal points is necesssary. However, increasing the number of grid points to keep the cell Peclet number constant is prohibitive because the velocities are proportional to the power of the Rayleigh number. The 70×34 nodal points were used for Ra numbers from 10^6 to 10^8 and 138×66 nodal points were used for Ra numbers from 10^8 to 10^{10}. The predicted value of average Nusselt number, $\overline{Nu}$, using the smaller number of nodes was 1.4% smaller than those with the larger number of nodes at $Ra = 1 \times 10^8$ for a fully liquid filled cavity. For a partially and fully porous medium case, the differences in predicted values were smaller at the same Ra number. The calculations were started with $Ra = 1 \times 10^6$, and subsequent calculations were with one order higher Ra numbers using the previous solution as the initial approximation. The required calculation times on a CYBER 205 computer ranged between 100 and 2000 CPU s.

RESULTS AND DISCUSSION

Experiments were conducted for two different aspect ratios of the test cavity, seven different porous matrix configurations, two different saturating fluids and three different temperature differences. The experimental conditions and relevant dimensionless parameters selected for the validation of the mathematical model are summarized in Table 1. The relatively small range of anisotropy in the permeabilities is due to the finite thickness and the large permeability of perforated plates forming the porous matrix. Also, changes in the porosity and the effective thermal conductivity are small. The results of flow visualization and temperature measurements with the pertinent numerical predictions are presented in Figs. 2–7. The effect of anisotropic permeability over a wide range of model parameters is further investigated via the numerical experiments and the results are presented in Figs. 8–10.

Flow structure

Flow visualization utilizing the electrolysis dye generation technique revealed the flow structure clearly.

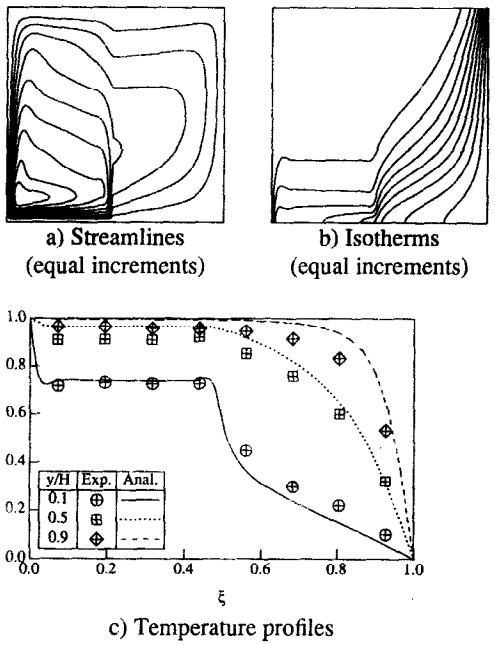

FIG. 2. Experimental and predicted results of experiment 1.

The resistance offered by the porous medium occupying half of the cavity, causes the shape of the streamlines to be quite different than those for a fully liquid or fully porous medium filled cavity. In all cases, the core of the convection cell is off-center towards the lower-left corner of the cavity, accompanied by the relatively strong boundary-layer type upward flow along the hot wall and almost horizontal flow near the bottom wall of the liquid reservoir. Due to the

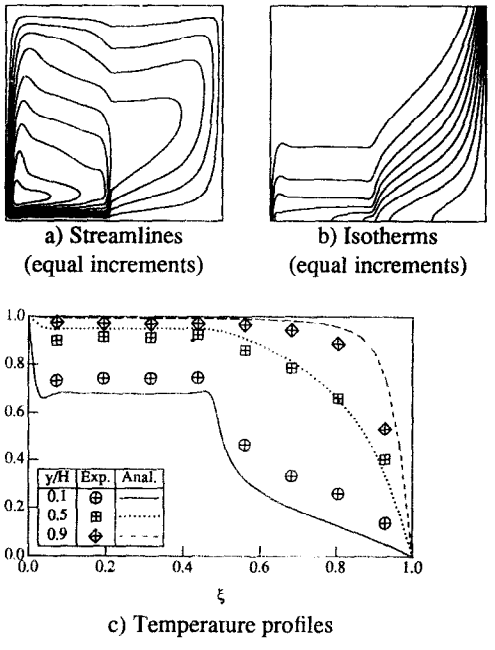

FIG. 3. Experimental and predicted results of experiment 2.

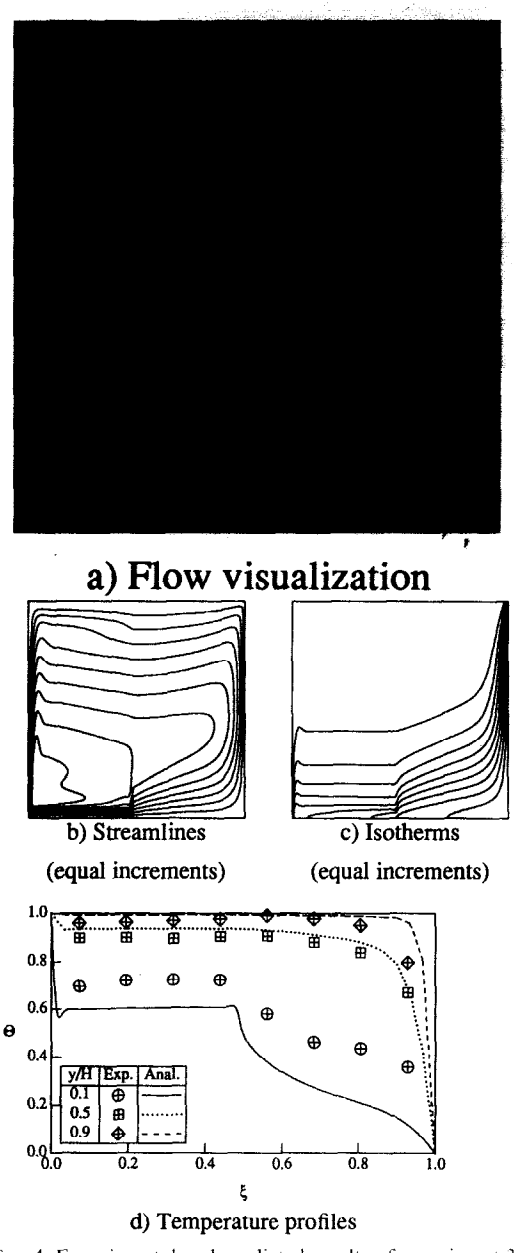

FIG. 4. Experimental and predicted results of experiment 3.

large velocities, the dye concentration is low near the walls and it is difficult to see the streamlines in the photographs.

In the porous medium, flow is relatively weak and is roughly towards the cold wall in the upper half and towards the hot wall in the lower half of the cell (Figs. 4a, 5a, 6a and 7a). The streamlines wiggle near the permeable plates forming the porous matrix, because the flow parallel to the plates is depressed as the fluid passes through the holes of finite depth. The flow directions are closer to the horizonal line as the Rayleigh number is increased and/or the x-direction permeability is increased. As the fluid exits from the porous medium and enters the liquid reservoir, the streamlines are distorted downward rather strongly (Fig. 4a). This is partly due to the anisotropy caused by the discontinuity in the flow characteristics [4] and partly due to the downward flow in the liquid reservoir near the interface which could not penetrate into the porous medium. Similar distortions are also observed when the liquid reservoir fluid penetrates into the porous medium, but are much weaker. This downward distortion brings the streamlines closer to the bottom connecting wall, and the fluid is accelerated towards the hot wall.

The flow structure in the liquid reservoir away from the hot wall and the bottom wall is subject to the changes in the experimental conditions. Some of the fluid, flowing along the top wall towards the cold wall, reverses its directions and returns all the way back to the vicinity of the hot wall and forms a flat convection roll occupying the upper part of the liquid reservoir when the aspect ratio was 2.14 (Fig. 6a). The vertical thickness of this secondary convection cell becomes smaller as the Rayleigh number is increased and/or the x-direction permeability is increased. At a Rayleigh number of 1.64×10^9, the flow in the liquid reservoir far from the hot wall is roughly towards the hot wall in the lower half and towards the cold wall in the upper half, except in the region occupied by the flat upper cell described above (Fig. 7a). For the smaller Rayleigh number, most of this region is occupied by a weakly recirculating flow, and the streamlines meander and even show oscillatory behavior (tangled streaks in Figs. 4a and 5a).

According to the numerical predictions, the penetration of the liquid reservoir flow into the porous layer is more significant when the Rayleigh number is larger (compare Fig. 2b with Fig. 4b and Fig. 5b with Fig. 7b), when the permeability is larger (compare Fig. 2b with Fig. 3b and Fig. 5b with Fig. 6b), and when the aspect ratio is smaller (compare Fig. 4b with Fig. 5b). The meander of the predicted streamlines in the core region of the convection cell and near the top wall of the liquid reservoir becomes strong as the Rayleigh number is increased. At a certain value of the Rayleigh number, meander near the top wall separates to form the flat upper cell described above. With further increase of the Rayleigh number, the shape of meanders in the core region become more complicated and another small but strong convection cell appears at the upper-left corner of the reservoir (Fig. 7b). At a high Rayleigh number ($Ra = 1 \times 10^{10}$), the cell at the lower-left corner vanishes, and the cell at the upper-left hand corner becomes dominant (Fig. 8c).

Temperature distributions

Shown in Figs. 2b, 3b, 4c, 5c, 6c and 7c are the predicted isotherms. For the ranges of the dimensionless parameters overlapping the present experimental conditions, the temperature distribution in the liquid reservoir is almost stratified except in the thin thermal boundary layer developed along the hot wall, indicating strong advective heat transfer. In the

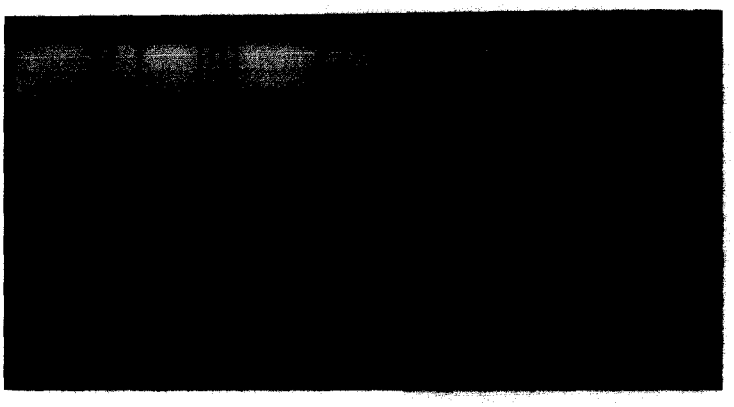

a) Flow visualization

FIG. 5. Experimental and predicted results of experiment 4.

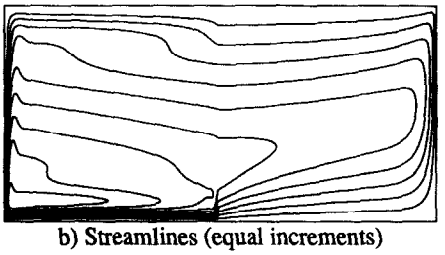

b) Streamlines (equal increments)

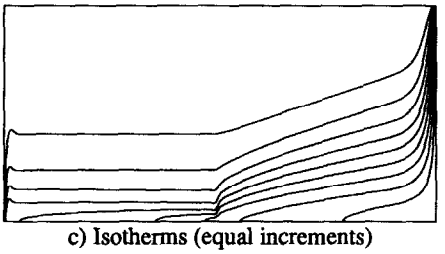

c) Isotherms (equal increments)

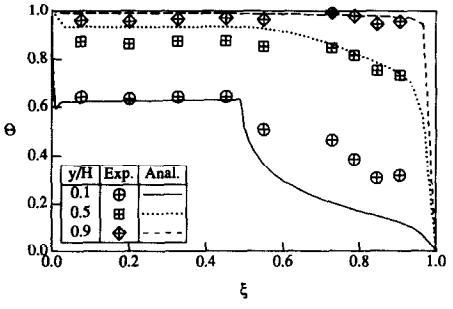

d) Temperature profiles

FIG. 5 *-continued.*

porous medium, the thermal boundary layer along the cold wall is thicker, and the horizontal component of the temperature gradient is comparable to the vertical component relatively far from the cold wall, due to the weak flow. However, the large changes in slope of the isotherms in the x-direction near the wall implies that advection is still an important heat transfer mode. When the penetration of the liquid reservoir flow into the porous layer becomes more significant, the isotherms in the porous media relatively far from the cold wall become more horizontal, and the temperature distribution in the porous region resembles that of the liquid reservoir (Fig. 7c). Near the interface between the liquid reservoir and the porous medium, the average vertical temperature gradient in the liquid reservoir is smaller than that in the porous medium. While the horizonal temperature gradient along the interface is almost zero for the upper half of the test cavity, the temperature drastically changes across the interface near the bottom connecting wall where the downward distortion of the flow is taking place. This drastic temperature change across the interface near the bottom wall is weaker when the penetration of the liquid reservoir flow into the porous medium is stronger.

Quantitative comparisons between measured and predicted temperatures are made in Figs. 2c, 3c, 4d, 5d, 6d and 7d, and reveal a relatively good agreement. The major discrepancies between the measured and predicted temperature profiles in the porous medium are found at $y/H = 0.1$. The lower and less uniform temperature profiles in the porous medium are predicted by the continuum model, which assumes periodically repeating permeable plate and voids as a homogeneous porous medium. In the thin layer adjacent to the cold wall and occupied by the permeable plate, the overall heat transfer coefficients are overpredicted. Firstly, because the predicted downward flow in this layer is suppressed in the real structure due to the perforated geometry of the permeable plates. Secondly, because the effect of the poor thermal conductivity of the solid matrix (0.121 W m^{-1} K^{-1}) is not localized in this layer, where the conduction heat transfer plays an important role, but is weakened by incorporating a homogeneous effective thermal conductivity. In the region far from the walls, the overall heat transfer coefficients are underpredicted, since the calculated meander of the flow in the liquid reservoir is weaker and the wiggle of the flow near the permeable plate cannot be mimicked with the continuum porous medium model. The discrepancies are larger when the permeable plate spacings are larger (compare Fig. 2c

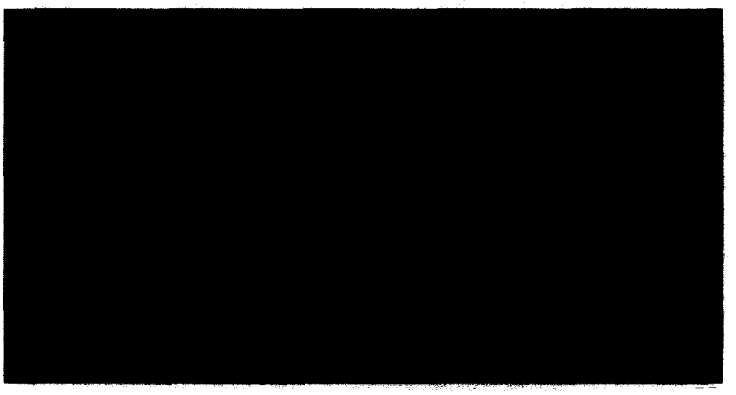

a) Flow visualization

FIG. 6. Experimental and predicted results of experiment 5.

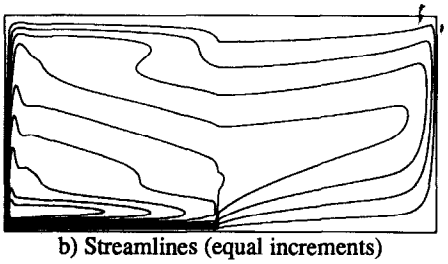

b) Streamlines (equal increments)

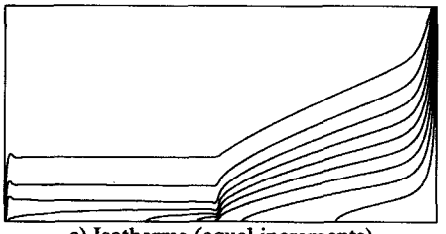

c) Isotherms (equal increments)

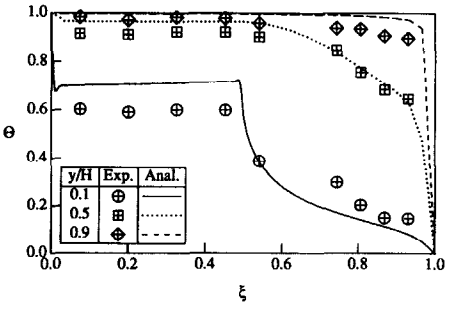

d) Temperature profiles

FIG. 6—*continued.*

with Fig. 3c and Fig. 5d with Fig. 6d). A better agreement could have been obtained, if the characteristic lengths and the spacings of the permeable plates had been smaller and/or more realistic models had been used.

At the other locations, $y/H = 0.5$ and 0.9, the measured temperatures are lower than predicted ones and are closer to room temperature. Conduction heat transfer through the sheathing of thermocouples affected the adiabatic boundary condition. Because the average temperature along the top wall is close to the hot wall temperature whereas near the bottom wall it is close to the room temperature, the measured temperatures at the upper part of the cavity were more affected by the heat loss to the ambient area. The temperature difference between the thermocouple bead and the surrounding fluid has been estimated to be small. Other minor sources contributing to the discrepancy are presumed to be the errors in evaluating the flow characteristics and the effective thermophysical properties of the porous medium.

The discrepancies between the experimental data and predicted results examined suggest that the mathematical model developed is a sufficiently reliable tool for investigating the effect of anisotropy on fluid flow and heat transfer in an enclosure partially filled with a porous medium for a wider range of dimensionless parameters.

Results of parametric studies

Among the dimensionless parameters which affect the flow and heat transfer are the Rayleigh number (Ra), D'Arcy number (Da) and the inverse ratio of x-direction and y-direction permeabilities to the reference permeability used in the D'Arcy number (R_{P_x} and R_{P_y} each). To accommodate the wide range of parameters in possible applications, the above dimensionless parameters were varied by four orders of magnitude in the numerical experiments. The aspect ratio and the ratio of the liquid reservoir thickness to the width of enclosure were fixed ($A = 2$ and $b = 0.5$). The Prandtl number was fixed at 5.0 ($Pr = 5$), and other dimensionless effective diffusion coefficients were taken as unity ($R_\mu = R_{k_x} = R_{k_y} = 1$). Also, the porosity was fixed at 0.75 ($\varepsilon = 0.75$), and the Forchheimer extension was not incorporated in the model ($f = 0$).

The average Nusselt numbers ($\overline{Nu}$) for the enclosure half-filled with an isotropic porous medium are compared to those of the fully liquid filled enclosure and fully porous medium filled enclosure (Fig. 9) for different Rayleigh numbers. The results also provide

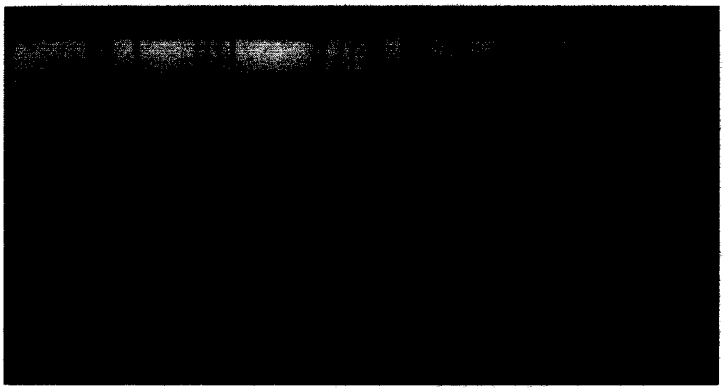

a) Flow visualization

FIG. 7. Experimental and predicted results of experiment 6.

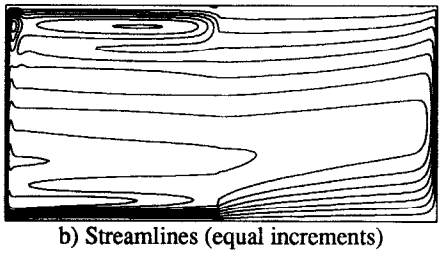

b) Streamlines (equal increments)

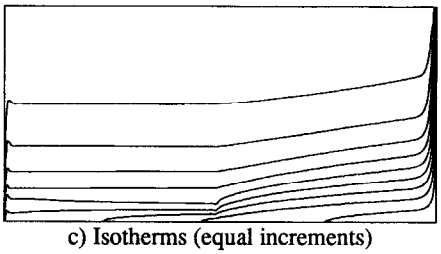

c) Isotherms (equal increments)

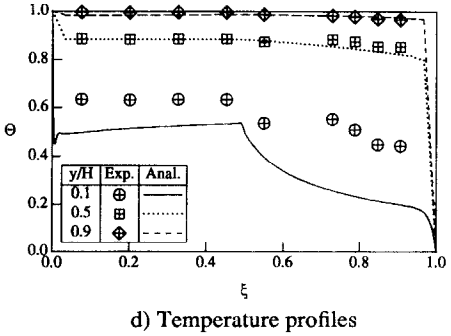

d) Temperature profiles

FIG. 7 *continued.*

the measure of the relative importance when the effects of anisotropic permeability on the average Nusselt number are examined. Over the range of the Rayleigh numbers considered, the average Nusselt number for a fully liquid filled enclosure is proportional to the power of the Rayleigh number [30], while such an expression for the Nusselt number is not appropriate for the partially or fully porous medium filled enclosure. At a given Rayleigh number, the average Nusselt number of the partially porous medium filled enclosure is closer to that of fully porous medium filled enclosure, implying that the thermal resistance of porous medium is greater than that of liquid reservoir. The streamlines and isotherms for three cases designated by a, b and c are given in Fig. 8a–c. At a lower Rayleigh number (1×10^6), the flow is confined to the liquid reservoir, and heat transfer in the porous medium is mainly by conduction. As the Rayleigh number is increased, the penetration of the liquid reservoir flow into the porous medium is increased, and the flow in the porous medium becomes gradually stronger. For $Ra = 1 \times 10^{10}$ the temperature field in the porous medium is stratified also. Note that only one strong convection cell exists at the upper left-hand corner of the cavity. The results for the enclosure half-filled with an isotropic medium are consistent with those reported in the literature [15], who claimed that the product of the Rayleigh and D'Arcy numbers should be greater than about 50 in order for penetration to be significant. Quantitative comparison of the results are not made because the parameters such as the Prandtl number and the aspect ratio are different.

The effect of anisotropy changes on the average Nusselt number was investigated at $Ra = 1 \times 10^8$, and the results are shown in Fig. 10. Either horizontal (dashed line) or vertical (solid line) permeability was varied, while the permeability in the other direction was fixed at the reference value equivalent to $Da = 1 \times 10^{-6}$. The abscissa is the dimensionless permeability, i.e. the inverse of either R_{P_Y} or R_{P_Y}. Thin horizontal lines denote the average Nusselt numbers for the enclosure partially filled with an isotropic porous medium for the D'Arcy numbers indicated. The change in the average Nusselt number resulting from one order decrease in the horizontal permeability (point e in Fig. 10) is noticeably larger than that resulting from the one order decrease in the vertical permeability (point d in Fig. 10). The streamline and isotherm patterns of those cases reveal that the flow in the porous medium is just strong enough to affect the heat transfer (Fig. 8d and e). A further decrease

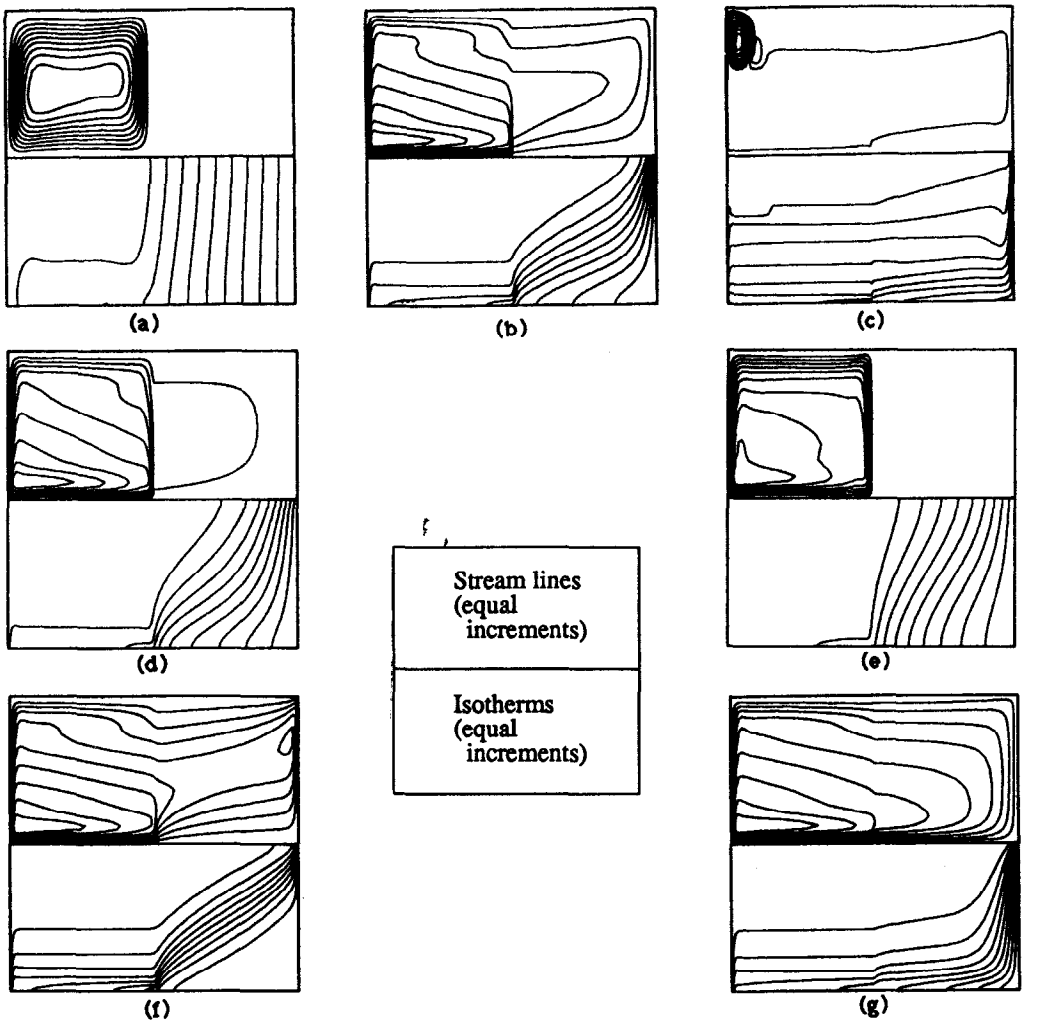

FIG. 8. Results of numerical experiments (conditions in Table 3).

of either the vertical or the horizontal permeabilities resulted in similar values of the average Nusselt number, because the flow intensity in the porous medium is further decreased and plays an insignificant role on heat transfer. The effect of increasing the vertical or the horizontal permeability on the average Nusselt number is almost equivalent to the effect of increasing the other permeability, because the flow in the porous medium is more controlled by the smaller permeability, and the average Nusselt number is a weak function of the anisotropy when the smaller permeability is fixed. However, the velocity and temperature distributions in the porous medium can be quite different even for the cases where predicted average Nusselt numbers are similar (Fig. 8f and g). A consistent averaging method to determine the equivalent isotropic permeability which would yield the same average Nusselt number over the range is not possible, and the effect of anisotropic permeability can be handled only by the appropriate mathematical models which account for the anisotropic flow characteristics. If an anisotropic permeability is approximated by an isotropic one having the value of geometric mean, the average Nusselt number can be greatly overpredicted as the smaller directional permeability is more representative of the flow characteristics.

During the solidification of castings, the transport equations governing the temperature, composition and flow fields are coupled through the mixture phase change model and many other physical phenomena such as nucleation and growth of floating crystals and channel type segregation, which also influence with those fields. Since the velocity and temperature distributions in the porous medium are strongly affected by the anisotropic characteristics, the importance of incorporating appropriate mathematical models which account for the anisotropic characteristics of porous media is emphasized.

CONCLUSIONS

Natural convection fluid flow and heat transfer inside a rectangular enclosure partially filled with an

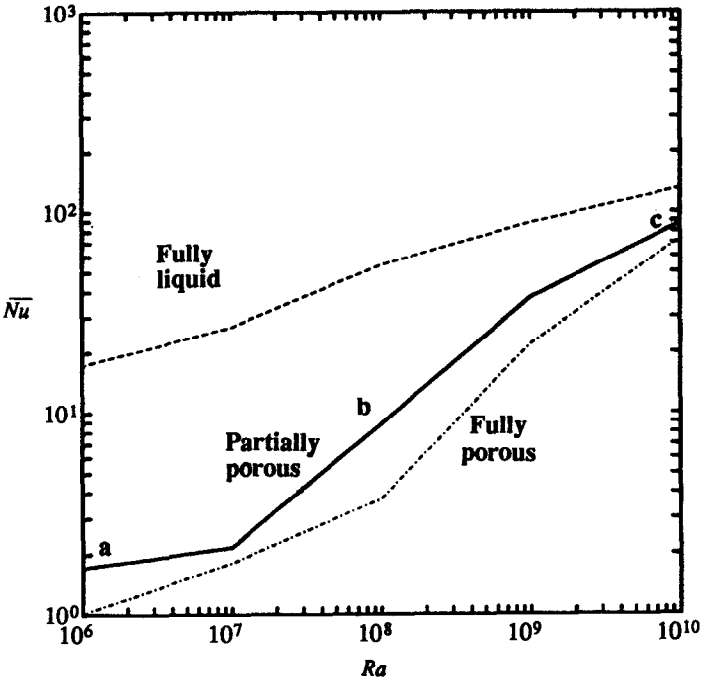

FIG. 9. Effect of the Rayleigh number on the average Nusselt number ($Pr = 5$, $Da = 1 \times 10^{-6}$, $R_{P_x} = R_{P_y} = 1$).

anisotropic medium was investigated experimentally and theoretically. Flow visualization utilizing the electrolysis dye generation revealed the flow structure clearly. At $Ra = 3.3 \times 10^7$, the liquid reservoir was largely occupied by the convection cell consisted of the boundary layer type horizontal flow along the bottom and upward flow along the hot wall of the cavity, together with the slow meandering flow far from the walls. According to the numerical predictions, the penetration of the liquid reservoir flow into the porous layer is more significant when the Rayleigh number of the permeability is larger and when the aspect ratio of

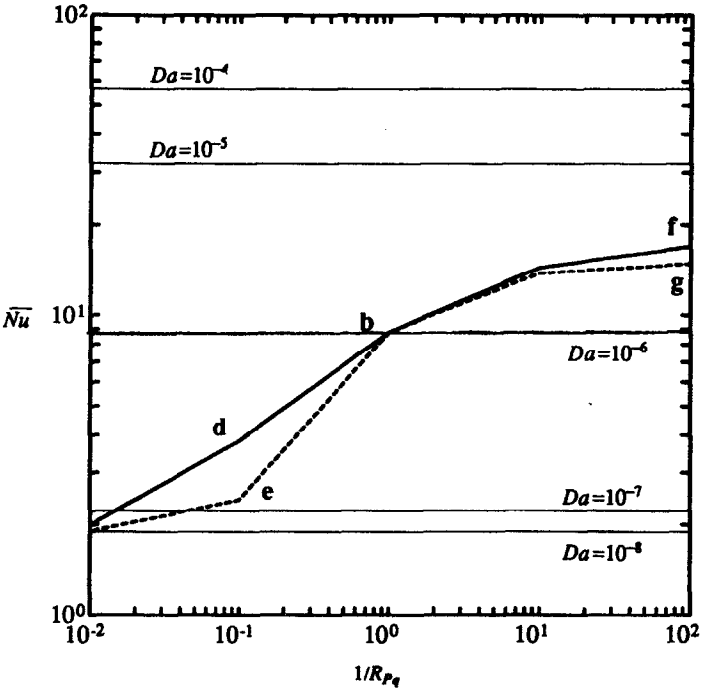

FIG. 10. Effect of anisotropic permeability on the average Nusselt number ($Pr = 5$, $Ra = 1 \times 10^8$, $Da = 1 \times 10^{-6}$).

Table 3. Summary of conditions for numerical experiments

	Ra	R_{P_x}	R_{P_y}
(a)	1×10^6	1.0	1.0
(b)	1×10^8	1.0	1.0
(c)	1×10^{10}	1.0	1.0
(d)	1×10^8	1.0	10.0
(e)	1×10^8	10.0	1.0
(f)	1×10^8	1.0	0.01
(g)	1×10^8	0.01	1.0

the test cavity is smaller. At $Ra = 2.5 \times 10^8$, another flat cell was observed near the top connecting wall. At even higher Rayleigh number ($Ra = 1.6 \times 10^9$), streamlines in the liquid reservoir were almost horizontal and flow was roughly towards the hot wall in the lower half and towards the porous medium in the upper half of the cavity. The upper cell also existed but was thinner than it was at a lower Rayleigh number. In the porous medium, flow was roughly towards the cold wall in the upper half and towards the liquid reservoir in the lower half. Streamlines were not smooth near the permeable plates forming the porous matrix. Chaotic flow patterns inside the lattice such as recirculations or meanders were weak far from the cold wall. Near the lower part of the interface between the liquid reservoir and the porous medium, the measured temperature changed drastically and the strong downward distortions of streamlines were observed on the liquid reservoir side. Measured temperature profiles implied that heat transfer was mainly by the convection both in the liquid reservoir and the porous medium at the experimental conditions studied.

A mathematical model based on the volume-averaged conservation equations has been developed and the results yielded agreed reasonably well with the experimental data. The overall heat transfer coefficients were overpredicted in the thin layer adjacent to the cold wall and occupied by the permeable plate, because the predicted downward flow in this layer is suppressed in the experiment due to the perforated geometry of the permeable plates used, and the effect of the poor thermal conductivity of the solid matrix is weakened as the homogeneous effective thermal conductivity model is utilized. In the region far from the walls, the overall heat transfer coefficients are underpredicted, since the predicted meander of the flow in the liquid reservoir is weaker and the wiggle of the flow near the permeable plate cannot be simulated. As the discrepancies between the predictions and the experimental data originate mainly from the homogeneous porous medium assumption of periodically repeating permeable plates and voids, a better agreement is expected when the characteristic lengths and spacings of the permeable plates are smaller.

To investigate the effect of anisotropic permeabilities for a wider range of dimensionless parameters, numerical experiments were conducted. At a given Rayleigh number, the average Nusselt number of the partially porous medium filled enclosure is closer to that of fully porous medium filled enclosure, implying that the thermal resistance of porous medium is greater than that of liquid reservoir. The effect of anisotropic permeability on the average Nusselt number is most significant when the flow is just strong enough to affect the heat transfer. For the physical system considered, the smaller directional permeability has greater control of the average Nusselt number as the anisotropy is increased. Consistent averaging method to determine the equivalent isotropic permeability which would yield the same average Nusselt number over the range is not possible. Differences in the velocity and temperature fields predicted for different ratio of directional permeabilities also suggest the need to incorporate the appropriate mathematical model which accounts for the anisotropic characteristics of the mushy zone in the analysis of solidifying castings.

REFERENCES

1. E. M. Sparrow, J. W. Ramsey and R. G. Kemink, Freezing controlled by natural convection. *J. Heat Transfer* **101,** 578–584 (1979).
2. M. Combarnous and D. Bernard, Modeling of free convection in porous media: from academic cases to real configurations, *Proceedings of the* 1988 *National Heat Transfer Conference, Houston* (Edited by H. R. Jacobs), HTD-Vol. 96-1, pp. 735–745. ASME, New York (1988).
3. J. H. Cushman and H. John, *Dynamics of Fluids in Hierarchical Porous Media*, Chap. 1. Academic Press, London (1990).
4. K. M. Gjerde and P. A. Tyvand, Thermal convection in a porous medium with continuous periodic stratification, *Int. J. Heat Mass Transfer* **27,** 2289–2295 (1984).
5. G. Castinel and M. Combarnous, Natural convection in an isotropic porous layer, *Int. Chem. Engng* **17,** 605–616 (1977).
6. K. N. Mehta and K. Nandakumar, Natural convection with combined heat and mass transfer buoyancy effects in nonhomogeneous porous media, *Int. J. Heat Mass Transfer* **30,** 2651–2655 (1987).
7. D. Poulikakos and A. Bejan, Natural convection in vertically and horizontally layered porous media heated from the side, *Int. J. Heat Mass Transfer* **26,** 1805–1813 (1983).
8. R. McKibbin and P. A. Tyvand, Thermal convection in a porous medium with horizontal cracks, *Int. J. Heat Mass Transfer* **27,** 1007–1023 (1984).
9. P. H. Oosthuizen and J. T. Paul, Free convection flow in a cavity filled with a vertically layered porous medium. *Proceedings of the 4th AIAA/ASME Thermophysics and Heat Transfer Conference, Boston* (Edited by V. Prasad and N. A. Hussain), HTD-Vol. 56, pp. 75–84. ASME, New York (1986).
10. P. Vasseur, C. H. Wang and M. Sen, Thermal instability and natual convection in a fluid layer over a porous substrate, *Wärme- und Stoffübertragung* **24,** 337–347 (1989).
11. C. W. Somerton and I. Catton, On the thermal instability of superposed porous and fluid layers, *J. Heat Transfer* **104,** 160–165 (1982).
12. D. Poulikakos, Thermal instability in a horizontal fluid layer superposed on a heat-generating porous bed, *Numer. Heat Transfer* **12,** 83–99 (1987).
13. D. C. Reda, natural convection experiments in a strati-

fied liquid saturated porous medium, *J. Heat Transfer* **108,** 660–666 (1986).
14. E. A. Ellinger and C. Beckermann, Melting of a pure substance in an enclosure partially occupied by a horizontal porous layer, *Proceedings of the 5th AIAA/ASME Thermophysics and Heat Transfer Conference, Seattle* (Edited by K. Vafai), HTD-Vol. 132, pp. 9–16. ASME, New York (1990).
15. C. Beckermann, S. Ramadhyani and R. Viskanta, Natural convection flow and heat transfer between a fluid layer and a porous layer inside a rectangular enclosure, *J. Heat Transfer* **109,** 363–370 (1987).
16. E. Arquis and J. P. Caltagirone, Interacting convection between fluid and open porous layers, ASME paper No. 87-WA/HT-24 (1987).
17. C. Beckermann, R. Viskanta and S. Ramadhyani, Natural convection in vertical enclosure containing simultaneously fluid and porous layers, *J. Fluid Mech.* **186,** 257–284 (1988).
18. Z. G. Du and E. Bilgen, Natural convection in vertical cavities with partially filled heat-generating porous medium, *Numer. Heat Transfer* **18A,** 371–386 (1990).
19. T. W. Tong, M. A. Faruque, S. Orangi and S. B. Sathe, Experimental results for natural convection in vertical enclosures partially filled with a porous medium, *Proceedings of the 4th AIAA/ASME Thermophysics and Heat Transfer Conference, Boston* (Edited by V. Prasad and N. A. Hussain), HTD-Vol. 56, pp. 85–93. ASME, New York (1986).
20. H. Campos, J. C. Morales, U. Lacoa and A. Campo, Thermal aspects of a vertical annular enclosure divided into a fluid region and a porous region, *Int. Comm. Heat Mass Transfer* **17,** 343–354 (1990).
21. D. R. Poirier, Permeability for flow of interdendritic liquid in columnar dendritic alloys, *Metall. Trans.* **18B,** 245–255 (1987).
22. R. West, Effect of gravity on the solidification of binary alloys—a numerical simulation, *Acta Astronautica* **13,** 735–738 (1986).
23. M. Song, Dendritic solidification of an anisotropic porous medium, Ph.D. Thesis, Purdue Univ., West Lafayette, IN (1993).
24. W. Merzkirch, *Flow Visualization*, Chap. 2, pp. 45. Academic Press, Orlando (1987).
25. M. L. Hunt and C. L. Tien, Effect of thermal dispersion on forced convection in fibrous media, *Int. J. Heat Mass Transfer* **31,** 301–309 (1988).
26. G. Neale and W. Nader, Practical significance of Brinkman's extension of Darcy's law, *Can. J. Chem. Engng* **52,** 475–478 (1974).
27. J. Bear and Y. Bachmat, *Introduction to Modeling of Transport Phenomena in Porous Media.* Kluwer Academic, Dordrecht, Netherlands (1990).
28. J. P. Doormaal and G. D. Raithby, Enhancements of the SIMPLE method for predicting incompressible fluid flow, *Numer. Heat Transfer* **7,** 147–163 (1874).
29. R. A. W. M. Henkes and C. J. Hoogendoorn, Comparison of turbulence models for the natural convection boundary layer along a heated vertical plate, *Int. J. Heat Mass Transfer* **32,** 157–169 (1989).
30. H. Ozoe, A. Mouri, M. Ohmuro, S. W. Churchill and N. Lior, Numerical calculations of laminar and turbulent natural convection in water in rectangular channels heated and cooled isothermally on the opposing vertical walls, *Int. J. Heat Mass Transfer* **28,** 125–138 (1985).